



AFRL-RX-WP-TP-2012-0391

**MECHANISMS OF PRECIPITATION OF DIFFERENT
GENERATIONS OF γ' PRECIPITATES DURING
CONTINUOUS COOLING OF A NICKEL BASE
SUPERALLOY (PREPRINT)**

**J. Tiley and G. B. Viswanathan
Metals Branch
Structural Materials Division**

**S. Nag, R. Banerjee, and A.R.P. Singh
University of North Texas**

**S. Chattopadhyay and Y. Ren
Illinois Institute of Technology**

**H.L. Fraser
The Ohio State University**

**AUGUST 2012
Interim**

Approved for public release; distribution unlimited.

See additional restrictions described on inside pages

STINFO COPY

**AIR FORCE RESEARCH LABORATORY
MATERIALS AND MANUFACTURING DIRECTORATE
WRIGHT-PATTERSON AIR FORCE BASE, OH 45433-7750
AIR FORCE MATERIEL COMMAND
UNITED STATES AIR FORCE**

REPORT DOCUMENTATION PAGE					Form Approved OMB No. 0704-0188	
<p>The public reporting burden for this collection of information is estimated to average 1 hour per response, including the time for reviewing instructions, searching existing data sources, gathering and maintaining the data needed, and completing and reviewing the collection of information. Send comments regarding this burden estimate or any other aspect of this collection of information, including suggestions for reducing this burden, to Department of Defense, Washington Headquarters Services, Directorate for Information Operations and Reports (0704-0188), 1215 Jefferson Davis Highway, Suite 1204, Arlington, VA 22202-4302. Respondents should be aware that notwithstanding any other provision of law, no person shall be subject to any penalty for failing to comply with a collection of information if it does not display a currently valid OMB control number. PLEASE DO NOT RETURN YOUR FORM TO THE ABOVE ADDRESS.</p>						
1. REPORT DATE (DD-MM-YY) August 2012		2. REPORT TYPE Technical Paper		3. DATES COVERED (From - To) 1 July 2012 – 1 August 2012		
4. TITLE AND SUBTITLE MECHANISMS OF PRECIPITATION OF DIFFERENT GENERATIONS OF γ' PRECIPITATES DURING CONTINUOUS COOLING OF A NICKEL BASE SUPERALLOY (PREPRINT)				5a. CONTRACT NUMBER FA8650-08-C-5226		
				5b. GRANT NUMBER		
				5c. PROGRAM ELEMENT NUMBER 62102F		
6. AUTHOR(S) J. Tiley and G. B. Viswanathan (AFRL/RXCM) S. Nag, R. Banerjee, and A.R.P. Singh (University of North Texas) S. Chattopadhyay and Y. Ren (Illinois Institute of Technology) H.L. Fraser (The Ohio State University)				5d. PROJECT NUMBER 4347		
				5e. TASK NUMBER		
				5f. WORK UNIT NUMBER X06B		
7. PERFORMING ORGANIZATION NAME(S) AND ADDRESS(ES) University of North Texas Corner of Ave C Chestnut Denton, TX 76203				8. PERFORMING ORGANIZATION REPORT NUMBER AFRL-RX-WP-TP-2012-0391		
9. SPONSORING/MONITORING AGENCY NAME(S) AND ADDRESS(ES) Air Force Research Laboratory Materials and Manufacturing Directorate Wright-Patterson Air Force Base, OH 45433-7750 Air Force Materiel Command United States Air Force				10. SPONSORING/MONITORING AGENCY ACRONYM(S) AFRL/RXCM		
				11. SPONSORING/MONITORING AGENCY REPORT NUMBER(S) AFRL-RX-WP-TP-2012-0391		
12. DISTRIBUTION/AVAILABILITY STATEMENT Approved for public release; distribution unlimited. Preprint to be submitted to Acta Materialia.						
13. SUPPLEMENTARY NOTES The U.S. Government is joint author of this work and has the right to use, modify, reproduce, release, perform, display, or disclose the work. PA Case Number and clearance date: 88ABW-2012-2971, 21 May 2012. This document contains color.						
14. ABSTRACT This paper focuses on developing a mechanistic understanding of the process of multiple nucleation bursts leading to the formation of multiple generations (or populations) with different size distributions, of γ' precipitates during the continuous cooling of a commercially used nickel base superalloy. This mechanistic understanding has been developed based on a number of critical experimental results; direct observation of the multiple nucleation bursts during in situ x-ray diffraction studies in the synchrotron, characterization of the size distributions associated with the different populations of γ' precipitates by coupling multiple imaging techniques at the appropriate length scale, and detailed compositional analysis of the γ' precipitates as well as the γ matrix using atom probe tomography. These analyses reveal that while local compositional equilibrium appears to have been achieved near the γ'/γ interface for the first-generation of precipitates, a non-equilibrium long range diffusion profile in the γ matrix is retained during the process of continuous cooling which is largely responsible for the subsequent nucleation bursts at larger undercooling...						
15. SUBJECT TERMS nucleation, precipitation mechanisms, gamma prime						
16. SECURITY CLASSIFICATION OF:			17. LIMITATION OF ABSTRACT: SAR	NUMBER OF PAGES 34	19a. NAME OF RESPONSIBLE PERSON (Monitor) Jaimie Tiley 19b. TELEPHONE NUMBER (Include Area Code) N/A	
a. REPORT Unclassified	b. ABSTRACT Unclassified	c. THIS PAGE Unclassified				

Mechanisms of Precipitation of Different Generations of γ' Precipitates During Continuous Cooling of a Nickel Base Superalloy

A. R. P. Singh¹, S. Nag¹, S. Chattopadhyay², Y. Ren², J. Tiley³, G. B. Viswanathan³, H. L. Fraser⁴, and, R. Banerjee¹

¹Center for Advanced Research and Technology and
Department of Materials Science and Engineering
University of North Texas, Denton, Texas, U. S. A.

²CSRRI-IIT, MRCAT, Advanced Photon Source, Argonne National Laboratory, 9700 S. Cass Avenue, Argonne, Illinois 60439, USA & BCPS Department, Illinois Institute of Technology, Chicago, IL 60616, USA

³Materials and Manufacturing Directorate
Air Force Research Laboratory, Dayton, Ohio, U. S. A.

⁴Center for the Accelerated Maturation of Materials and
Department of Materials Science and Engineering
The Ohio State University, Columbus, Ohio, U. S. A.

Abstract

This paper focuses on developing a mechanistic understanding of the process of multiple nucleation bursts leading to the formation of multiple generations (or populations) with different size distributions, of γ' precipitates during the continuous cooling of a commercially used nickel base superalloy. This mechanistic understanding has been developed based on a number of critical experimental results; direct observation of the multiple nucleation bursts during in situ x-ray diffraction studies in the synchrotron, characterization of the size distributions associated with the different populations of γ' precipitates by coupling multiple imaging techniques at the appropriate length scale, and detailed compositional analysis of the γ' precipitates as well as the γ matrix using atom probe tomography. These analyses reveal that while local compositional equilibrium appears to have been achieved near the γ'/γ interface for the first-generation of precipitates, a non-equilibrium long range diffusion profile in the γ matrix is retained during the process of continuous cooling which is largely responsible for the subsequent nucleation bursts at larger undercooling (or lower temperatures) leading to the second and third generations of precipitates. Additionally, since these subsequent generations of precipitates are formed at larger undercoolings, they are highly refined, exhibit far-from equilibrium compositions, and also have very diffuse γ'/γ interfaces, indicating a non-classical precipitation mechanism associated with their formation.

Introduction

Nickel base superalloys possess an excellent balance of properties like high strength, ductility, fracture toughness, good fatigue and corrosion resistance, both at room as well as elevated temperatures. Due to these unique properties they have widespread application in a number of critical technological areas, especially those involving high temperatures such as aircraft jet engines. These properties in nickel base superalloys arise by the precipitation of the ordered γ' phase (in some cases both γ' and γ'' phases) within a disordered γ matrix. The microstructure of these alloys, especially in terms of the composition, morphology, spatial, and, size distributions of the γ' precipitates plays a very important role in determining the mechanical properties of these alloys [1-2]. Rene' 88 DT alloy is a recently developed nickel base superalloy that was developed [3-5] to be more damage tolerant than the previous generation Rene' 95 alloy, while offering improved creep strength and fatigue crack growth resistance [5]. The nominal chemistry for this alloy is: 13% Co, 16% Cr, 4% Mo, 4% W, 2.1% Al, 3.7 % Ti, 0.7% Nb, 0.03% C and 0.015% B. This alloy is typically processed through the powder metallurgy route and develops a polycrystalline microstructure consisting of γ grains with nanoscale γ' precipitates. Furthermore, the typical heat-treatment used for this alloy consists of a solutionizing procedure for 30 to 60 minutes at 1150°C (2100°F) in the single γ phase field, followed by continuous cooling to room temperature at appropriate cooling rates, and subsequent aging for different time periods at temperatures such as 760°C (1400°F).

The microstructural evolution in superalloys, such as Rene 88DT, during continuous cooling is strongly dependent on the cooling rate employed. Faster cooling rates, such as those encountered during water quenching the alloy from the high temperature single γ phase field, typically lead to the formation of a monomodal size distribution of refined γ' precipitates [6-8]. In contrast, relatively slower cooling rates lead to the formation of γ' precipitates with a bimodal size distribution or in some cases even a multi-modal size distribution [6,9-13]. The development of multiple populations of γ' precipitates during continuous cooling [10,12,13] or by isothermal annealing at two different temperatures [11,14], has often been attributed to multiple distinct bursts of nucleation of precipitates at different undercoolings below the γ' solvus. These multiple nucleation bursts in turn result from the complex interplay of continuously increasing thermodynamic driving force for nucleation (chemical free energy difference) due to increasing undercooling, reduction in this driving force due to previous nucleation events, and, the rapidly declining diffusivity of alloying elements with decreasing temperature. At lower undercoolings (or higher temperatures, just below the γ' solvus temperature) lower driving force for nucleation coupled with higher diffusivities leads to the first burst of γ' nucleation forming the first generation of precipitates with low nucleation density, often referred to as primary γ' precipitates. At higher undercoolings reduced diffusivity of atoms leads to supersaturation of γ' -forming elements away from the diffusion fields of the growing primary γ' precipitates, and coupled with a greater thermodynamic driving force results in further bursts of nucleation consequently forming secondary (or tertiary in some cases) γ' precipitates with a high nucleation density [6,10,11]. This mechanism has been discussed in the phase field modeling studies by Wen et.al. [10], where the

Ginzburg-Landau equation has been coupled with the non-linear Cahn-Hilliard diffusion equation. In order to simulate the precipitation sequence during continuous cooling of the Ni-Al alloy, a Langevin stochastic term was introduced while accounting for the contribution due to undercooling. Their results show a bimodal distribution of γ' particles with a significant gap between the two nucleation events. The shut off of nucleation at high temperatures could be attributed to the soft impingement (overlap of diffusion fields) of first generation γ' precipitates. At lower temperatures (higher cooling) due to increased supersaturation of elements like Ti and Al, in between the γ' free channels a subsequent nucleation event may take place. Similar studies have been done by Radis et. al. [12] where they have employed classical nucleation theory involving long range diffusion of atoms to understand nucleation kinetics of both monomodal as well as multimodal size distributions of γ' precipitates in the commercial nickel base superalloy Udimet 720. A slightly different approach was adopted by Boussinot et.al. [14], where phase field modeling was conducted to simulate isothermal annealing at two different temperatures, which led to nucleation of two different γ' generations. At a higher temperature the Ni-Al alloy was aged for a sufficiently long time period to permit equilibration of the far-field γ composition and volume fraction of γ and the first generation γ' precipitates. Subsequently on quenching to a lower temperature a second generation of γ' precipitates are formed that are considerably smaller in size and larger in number density when compared to the first generation precipitates. Further annealing at this temperature results in the growth of the smaller precipitates. However not all precipitates grow continuously. The smaller particles that are situated near the larger precipitates starts decreasing in size and eventually disappears at the expense of the growth and coarsening of latter. This diffusion mediated interaction of the two generations of γ' precipitates is strongly dependent on the volume fraction of the larger precipitates, that in turn governs the γ channel width within which subsequent precipitation may take place. A similar investigation was done by Wen et.al. [11] where the growth kinetics and evolution of precipitate number density with time was obtained by conducting isothermal annealing studies at different temperatures.

Three dimensional characterization of the morphology, size distribution, and, composition of γ' precipitates in Ni base alloys has been previously attempted via atom probe tomography (APT), for finer scale γ' precipitates, and, serial-sectioning in a dual-beam focused ion beam (FIB) for coarser scale γ' precipitates and these studies have been extensively reviewed in recent articles in the published literature [8, 15-17]. These studies have been primarily conducted during annealing after rapid quenching the alloy from the high temperature single γ phase field. Therefore, typically these studies have focused on a monomodal size distribution of refined γ' precipitates within the disordered γ matrix [8]. In addition, such APT studies have also focused on the partitioning of the alloying additions between these two phases and the segregation of certain alloying additions to the γ/γ' interface as well as to grain boundaries. Serial-sectioning and sequential SEM imaging, carried out using a dual-beam focused ion beam system, followed by 3D reconstruction, has also been recently used to investigate the three-dimensional morphology and distribution of larger scale primary γ' precipitates [18].

The above isothermal annealing studies, although quite important in understanding the nucleation and growth behavior of γ' precipitates, are quite different from the typical industrially relevant heat-treatments. In the later case, the cooling rates employed after solutionizing/homogenizing in the single γ phase field are substantially slower than water-quenching and therefore often lead to the formation of multiple size ranges of γ' precipitates. Therefore, the focus of the current paper is on determining the morphology, distribution and composition of multiple generations of γ' precipitates, of different size ranges, forming during continuous cooling of Rene 88DT as well as the compositional partitioning between these γ' precipitates and the adjoining γ matrix. The elemental partitioning as well as the 3D morphology of the finest scale of γ' precipitates has been primarily characterized by APT. While APT affords a nanometer scale resolution of structure and chemistry, it offers limited information in terms of the sampled volume of reconstruction and consequently is not the method of choice for analyzing coarser γ' precipitates. Thus in order to better understand the overall representative morphological features over larger length scales, SEM and EFTEM has been found to be a more suitable method [13,19]. The four primary objectives of this paper are as follows:

1. To identify the different generations of γ' precipitates that form during continuous cooling of a nickel base superalloy via in situ high energy x-ray diffraction studies carried out in a synchrotron.
2. Analysis of the size distribution and morphology of multiple generations of γ' precipitates, formed during continuous cooling at a relatively slow rate from the solutionizing temperature (single γ phase-field) using SEM and EFTEM.
3. Detailed compositional analysis of the different generations of γ' precipitates as well as their near and far field γ compositions using APT. Investigation of the γ - γ' compositional partitioning and associated diffusion fields and interface widths.
4. Develop a better physical understanding of the mechanism of γ' precipitation in these alloys as a function of undercooling (below the γ' solvus temperature).

Experimental Procedure

The bulk chemical composition of the commercially procured Rene 88 DT alloy was 56.53Ni-16.24Cr-13.27Co-3.92Ti-2.09Al-4.08Mo-3.92W-0.76Nb (wt%) or 55.63Ni-18.02Cr-13.00Co-4.74Ti-4.45Al-2.48Mo-1.21W-0.46Nb (at%). Material was cut from the bore and rim section of a disk, produced and tested under work supported by the Defense Advanced Research Projects Agency, Defense Sciences Office (Engine Systems Prognosis, Contract Nos. HR0011-04-C-0001 and HR0011-04-C-0002). The program evaluated the impact of microstructure on mechanical properties [20]. The samples were supersolvus solution treated in a vacuum furnace at 1150°C in the single γ phase field for 30 minutes to dissolve any existing γ' and then slow cooled at an average cooling rate of 24°C/min (to be subsequently referred to as SC0). These samples were subsequently aged for a period of 1 and 15 hours, at 760°C in a large chamber vacuum furnace and air quenched. Subsequently in this manuscript these samples would be referred to as SC1 and SC15 respectively.

For synchrotron studies, high-energy x-ray diffraction (HEXRD) was performed at beamline 11-ID-C at the Advanced Photon Source (APS) facility in Argonne National Laboratory. Beam energy of 115 keV (equivalent to a wavelength of 0.11 Å) and beam size of 0.5 mm by 0.5 mm was used for the diffraction studies. Rene 88DT samples, roughly 5 mm in diameter and 2 mm in thickness, were loaded in a Linkam TS1500TM furnace that was kept in an Argon atmosphere. The diffraction patterns were collected at a time interval of 30 secs with a Perkin-Elmer 2D detector located at a distance of 1.6 m from the sample.

Samples for APT studies were prepared by focused ion beam milling technique. For this purpose, samples were prepared by dual-beam focused ion beam (FIB) instrument (FEI Nova Nanolab 200) system using a Ga ion beam. The ion beam thinning was carried out in multiple steps, starting with 30 kV ions and finally finishing with 5 kV ions to reduce the surface damage caused by the higher energy ions [21]. The final tip diameter of the atom probe specimens was ~ 50 – 80 nm. The APT experiments were carried out using a LEAP 3000 local electrode atom probe (LEAPTM) system from Cameca Inc. All atom probe experiments were carried out in the electric-field evaporation mode at a temperature of 70 K, with the evaporation rate varying from 0.2 – 1.0 % and the pulsing voltage at 30% of the steady-state applied voltage.

TEM samples were also prepared via conventional routes, consisting of mechanical grinding and polishing of 3 mm diameter discs, followed by dimple grinding, and, final ion-beam milling to electron transparency. Ion beam milling was conducted on a Gatan Duo Mill and Fischione Model 1010 ion milling system, operated at 6 kV. TEM analysis was conducted on a FEI Tecnai F20 field emission gun transmission electron microscope operating at 200 kV. Images were obtained using the Cr M-edge (42 eV) in the energy filtered transmission electron microscopy (EFTEM) mode, as described elsewhere [19]. Representative regions were imaged at different magnifications to capture the relevant secondary and/or tertiary γ' precipitates in the alloy.

SEM analysis of primary γ' precipitates were done using backscattered detector on etched samples. Prior to SEM analysis the samples were polished and etched using Keller's reagent (15 ml HCl + 10 ml Glycerol + 5 ml HNO₃). This light etching substantially enhanced the contrast between the γ and γ' phases in the secondary electron imaging mode of the SEM.

Results and Discussion

In situ x-ray diffraction studies of nucleation of multiple generations of γ' precipitates

The γ' precipitation during slow continuous cooling of the Rene 88 alloy from above the γ' solvus temperature at the rate of 24°C/min, i.e. from the single γ phase field, has been investigated via in situ high energy x-ray diffraction studies, carried out using a high temperature furnace mounted on the synchrotron beam line at the Advanced Photon Source (APS) at the Argonne National Laboratory. The results of these diffraction studies have been summarized in Fig. 1. Fig. 1(a) and (b) show the progressive change in the

intensity of the (001) γ' superlattice, and (111) fundamental reflections arising from both γ and γ' phases, as a function of temperature during in situ slow continuous cooling from the single γ phase field. Fig 1(a) shows a sudden increase in (001) peak intensity during cooling between 1284°C and 1174°C, which then increases gradually with further reduction in temperature. The combined (111) reflection from γ' and γ phases show a gradual increase in intensity during the same cooling cycle as shown in Fig. 1(b). A simple first order approximation of the change in volume fraction of γ' as a function of temperature during continuous cooling, can be qualitatively measured by plotting the ratio of the intensities of (001) γ' peak to (111) $\gamma' + \gamma$ peak at every temperature, as shown in Fig 1(c). The plot clearly shows that during the cooling experiment, the intensity of the (001) γ' peak starts increasing at a temperature marginally higher than 1200°C, corresponding to the onset of the first nucleation burst. With decreasing temperature there is a continuous increase in the above intensity ratio, with a maxima at around 1000°C. On subsequent cooling, there is another increase in the intensity ratio with an onset at a temperature \sim 800°C with an actual maxima at around 700°C (Fig. 1(c)). These peaks observed in the (001) γ' peak to (111) $\gamma' + \gamma$ peak intensity ratio give an indication of various γ' nucleation bursts, eventually resulting in a multimodal size distribution of γ' precipitates. It is important to note that the relative increase in this intensity ratio is directly proportional to the volume fraction of newly formed γ' precipitates and with decreasing temperature, the relative increase in γ' volume fraction with each successive generation decreases. This is clearly seen from Fig. 1(c) where the increase in intensity, corresponding to the first nucleation burst, is significantly greater than that attributable to the second burst. Also, while only two distinct γ' nucleation bursts are visible in Fig. 1(c), a possible third burst at much lower temperatures cannot be ruled out since it possibly leads to a rather small, and consequently difficult to detect, change in the intensity ratio. Figs. 1(a) and (b) also show a systematic shift in the (001) γ' as well as (111) $\gamma' + \gamma$ intensity peaks, indicating a decrease in lattice parameter for both γ' and γ phases with decreasing temperature. This decrease in lattice parameters can possibly be attributed to the combined effect of thermal contraction and the chemical partitioning between γ' and γ phases. However, the changes in lattice parameters are not equal for γ' and γ phases as seen in Figs. 1(a) and (b), which gives rise to an increase in the γ'/γ lattice mismatch with decreasing temperature as reported previously for the Rene 88 alloy [22]. This also alludes to the fact the ordered γ' phase is more stable with respect to temperature changes and therefore the change in lattice parameter with temperature is minimal for this phase.

Precipitate size and morphology

Slow cooling (SC0) of Rene 88 from a temperature exceeding the γ' solvus resulted in a multimodal distribution of precipitates as mentioned earlier. This multimodal distribution of precipitates can be divided into different groups based on their size, morphology and number density. These parameters in turn depend on the undercooling corresponding to the specific nucleation event, resulting in that particular population of precipitates. The different populations of γ' precipitates were characterized by coupling backscatter SEM studies with EFTEM studies.

Figs. 2(a) and (b) show low and high magnification backscatter SEM images of the SC0 sample with γ' precipitates exhibiting a darker contrast. As seen from the figure, the larger first generation γ' precipitates develop largely a cuboidal morphology or in some cases an irregular morphology, due to coarsening or impingement of neighboring γ' precipitates. Henceforth, these first generation γ' precipitates, will be referred to as primary γ' precipitates. These primary γ' precipitates have a relatively low number density, attributable to the smaller driving force for nucleation expected at lower undercooling. This is also evident on comparison with second and third generations of γ' precipitates forming at larger undercoolings (lower temperatures). Furthermore, there is a large variation in shape and size of the primary γ' precipitates. The size distribution of primary γ' precipitates is shown in Fig. 4(a). The equivalent diameters of these γ' precipitates were determined by measuring their respective areas and equating these areas to areas of equivalent circles. Due to the irregular shape of these precipitates, this method really provides a qualitative rather than a quantitative distribution of precipitate sizes. As expected from the figure, there is a large variation in the sizes of these precipitates, ranging from 100-400 nm in diameter with the maximum number of precipitates lying in the size range of 150-250nm. Thus it is clear that the primary γ' precipitates of this size range can be analyzed based on SEM investigations.

The second generation, secondary γ' population, that nucleates at lower temperatures due to a very high thermodynamic driving force, grow at much lower rates due to the limited diffusivity at the lower temperatures. Imaging these rather small second generation γ' precipitates is difficult using SEM, and therefore EFTEM imaging was employed, as shown in Figs. 3(a) and (b). These EFTEM images are recorded using the Cr M-edge in the electron energy loss spectrum, obtained from the same sample. As observed in the images, the γ' precipitates exhibit a darker contrast being depleted in Cr [13,19]. As discussed earlier, the number density of the secondary γ' precipitates is clearly much larger than those of the primary γ' precipitates. This could be attributed to high nucleation rate at high undercoolings. Furthermore, as seen in the higher magnification EFTEM image in Fig. 3(b), the primary γ' precipitates are separated from the secondary γ' precipitates by a precipitate-free depleted zone. Due to limited growth these secondary γ' precipitates exhibit near-spherical morphologies with size ranging from 12-30nm in diameter. To clearly distinguish between the first and second generation of γ' precipitates, the size distribution for both precipitates have been also plotted in Fig. 4(a). At this scale of analysis, TEM imaging techniques like EFTEM is the most suitable technique to measure the size of these precipitates and consequently find out their statistical size distribution.

On careful study of the higher magnification EFTEM image in Fig. 3(b), a third population of extremely fine scale γ' precipitates is visible. These precipitates are present between the primary and secondary γ' precipitates, beyond the precipitate free zone that surrounds the primary γ' precipitates. The extremely small size of these precipitates, even smaller than the secondary ones, may be a result of a third burst of nucleation at much lower temperatures (even higher undercooling). Due to their very small size and the limitations of EFTEM imaging in terms of spatial resolution, it is very difficult to

accurately measure the size distribution of these precipitates using this technique.

Overall size distribution

The overall size distribution of different generations of γ' is shown in Figs. 4(a) and (b). As seen in these figures, both bursts of nucleation give rise to two distinctly different populations of γ' with each nucleation event probably occurring over a range of temperatures, starting with a high driving force for nucleation which gradually decreases. Both generations of γ' show similar distributions and have been fitted to classical Gaussian distributions in Fig. 4(b). The average diameter of the primary γ' precipitates is $\sim 191\text{nm}$ with standard deviation of $\sim 78\text{ nm}$ which is close to the fitted peak of the Gaussian at 188nm . Secondary γ' precipitates have average diameter of $\sim 8\text{nm}$ and a standard deviation of $\sim 7\text{nm}$ which is also close to the peak of the Gaussian at $\sim 9\text{nm}$ in Fig. 4(b). Therefore for both first and second generation of γ' precipitates, that were measured independently using SEM and EFTEM techniques respectively, the Gaussians are in close agreement with the actual frequency distributions. The salient points regarding the size distribution of γ' precipitates can be summarized as follows:

1. Second generation, secondary γ' precipitates, have a much higher number density as compared to primary γ' precipitates.
2. The distributions observed in this study also indicate that each nucleation burst occurs over a range of temperatures.
3. Within each temperature window for a specific generation of γ' precipitates, the larger number of precipitates nucleate at lower temperatures and a smaller number nucleate at higher temperatures.

As mentioned earlier, a third generation of (tertiary) γ' precipitates is also present in this SC0 sample. However the size distribution of the tertiary population cannot be accurately quantified using EFTEM. Thus only an average size of these precipitates could be determined and has been indicated by a dashed line in Fig. 4(b). In order to identify and characterize this third generation of γ' precipitates, isothermal studies were conducted on the SC0 sample. The results of these studies have been discussed later in the manuscript. The distribution also shows that the size difference between primary and secondary γ' is more as compared to secondary and tertiary γ' populations. This can be attributed to the higher diffusivity at high temperatures (where the primary precipitates form) leading to their more rapid growth while the growth of the secondary and tertiary precipitates is rather limited at their lower formation temperatures. While previously reported modeling studies, based on classical nucleation theory, predict the formation of these multiple generations of γ' precipitates and their size distributions [10-12] this study is one of the first reports presenting direct experimental evidence of the size distribution associated with different generations of γ' precipitates forming during continuous cooling of a nickel base superalloy.

Compositional analysis of different generations of γ'

The compositional analysis of different generations of γ' precipitates has been carried out

using atom probe tomography (APT). Fig. 5(a) shows a three-dimensional (3D) atom probe reconstruction of the SC0 sample. For simplicity, only two atomic species, Al and Cr, have been shown in the figure. The red ions represent Al ions whereas blue represent Cr ions. This reconstruction clearly shows that the Al and Cr partition to the γ' and γ phases respectively. A better visual representation of the same 3D reconstruction is shown in Fig. 5(b), where an iso-concentration surface (or isosurface in short) using 14at% Cr has been plotted along with the Ni ions (in green). This isosurface view clearly shows sections of two large primary (first-generation) γ' precipitates along with multiple fine scale γ' precipitates. Going by the size of these fine scale particles, they are either tertiary or secondary precipitates at the smaller end of their size distribution. These precipitates are also clearly visible from the EFTEM image in Fig. 3(b). A precipitate-free γ' depletion zone, containing only Ni ions, between the two different sizes of precipitates is also observed from the reconstructions in Fig. 5. A second atom probe reconstruction (Cr=14at% isosurface along with Ni ions) of the same SC0 sample is shown in Fig. 5(c). This figure also shows a section of a primary γ' precipitate, multiple tertiary (or secondary) γ' precipitates, and the precipitate-free zone in between.

The partitioning of the primary alloying elements in Rene' 88 DT alloy, i.e. Al, Ti, Cr, Co, and Mo, for two different generations of γ' precipitates is shown in the compositional profiles in Figs. 6(a) and (b) respectively. These compositional profiles, represented in the form of proximity histograms (or proxigrams corresponding to a Cr=14% isosurface) [23], clearly revealed that while all the γ' precipitates, represented by the left side of the plot in each case, are enriched in Al and Ti and depleted in Cr, Co and Mo. However from the steady state value on the left of the proxigrams, it can be said that the relative compositions of primary and tertiary (or secondary) precipitates is substantially different. Thus the primary γ' precipitates contain a higher amount of Al and Ti, whereas the tertiary γ' have lower Al and Ti and higher Co and Cr, as evident after comparing Figs. 6(a) and (b) respectively. Even though there is a variation in size of the smaller γ' precipitates, the variability in composition between different precipitates was observed to be minimal. This indicates that even though the tertiary (or secondary) precipitates form over a range of temperatures, large variations in composition within this particular generation does not occur. Fig. 6(c) compares the Al and Cr compositional profiles across the γ'/γ interface for a specific large (primary) and a small (tertiary or secondary) γ' precipitate. This comparison clearly reveals the substantially more diffuse interface in case of the smaller precipitates (plotted using dotted lines) as compared with the primary ones (plotted using bold lines). Similar evidence of a larger compositional width of the γ'/γ interface in case of smaller tertiary (or secondary) precipitates, indicating a compositionally diffuse interface, was observed in case of many other precipitates analyzed in the same manner. It should also be noted that in addition to the tertiary γ' precipitates clearly delineated from the γ matrix using the Cr-14at% isosurface construction, the raw ionic reconstruction, shown in Fig. 5(a) also reveals pockets of local enrichment of Al ions (in red) between tertiary γ' and the depletion zone. These small pockets are possibly far-from equilibrium in composition but still depleted in Cr and enriched in Al as compared to the γ matrix, and could potentially act as the nucleation sites for γ' .

While each generation of γ' has a different composition, the γ region near these γ' precipitates also exhibit local compositional variations. Fig. 7(a) shows a proxigram that is plotted across a primary γ' precipitate, on the left, to a precipitate-free γ' depletion zone towards the right. The plot shows the near-field and far-field compositions of the γ matrix. Right next to the primary γ' precipitate the γ matrix shows a near-equilibrium composition. From the plot it is evident that primary γ' precipitate (represented by the region on the left) contain higher amounts of Al and Ti whereas the depletion zone is enriched in Cr and Co. The compositional gradient across the interface also appears sharp. Mo partitioning across the interface is not large even though it seems to be partitioning more towards the γ matrix. From left to right, the proxigram shows a slight decrease in the Cr and Co content, suggesting a change in composition within the precipitate free γ matrix. Thus as one probes away from the primary γ' precipitate, the γ composition within the depletion zone also departs further away from equilibrium. This variation in composition within the γ matrix, near and away from the primary γ' precipitate, is also observed in the case of Al and Ti, as evident from the magnified view of the proxigram (Fig. 7(b)). It can be clearly seen that right next to the γ'/γ interface there is a local depletion of Al and Ti ($\sim 1\text{at}\%$ and $0.5\text{at}\%$ respectively) which gradually increases ($\sim 1.7\text{at}\%$ and $1\text{at}\%$ respectively) as one probes away from the primary γ' precipitate. Similar to Fig. 7(b), Fig. 7(c) shows a magnified view of the Cr composition profile across the γ'/γ interface. The trend followed by this plot is an inverse of the plots shown in Fig. 7(b). Thus, there is a local enrichment of Cr next to the interface ($\sim 30\text{at}\%$) which slowly decays to $\sim 27\text{at}\%$ inside the depletion zone. These observations show that in Rene' 88DT alloy there exists a compositional gradient within the precipitate free region of the γ matrix, where the composition of all the major alloying additions slowly change from near-equilibrium to far from equilibrium as one moves away from the interface into the γ matrix. However as expected, this gradient is much more diffuse in comparison to the compositional gradient observed across the γ'/γ interface. Additionally, it should be noted that the far-field composition of this precipitate free region within the γ matrix is enriched in Cr and Co, and depleted in Al and Ti, as compared to average alloy composition.

From Fig. 6 it is clear that the compositions of coarser and finer γ' precipitates are close to equilibrium, and far from equilibrium, respectively. However, a closer examination of the atom probe reconstruction in Fig. 5(a) showing the γ region near the depletion zone reveals some interesting details. Figs. 8(a) and (b) show 2-D compositional maps of Cr, created using a 2nm thick region of interest across primary and tertiary (or secondary) γ' precipitates, along with the depleted zone lying in between. These maps are pseudo-colored based on the composition, with color changes from blue to yellow to red, representing progressively increasing Cr content. While Fig. 8(a) shows the map with an overlapping 14at% Cr isosurface, Fig. 8(b) shows only the 2-D compositional map. Comparing the two figures, the primary γ' precipitate in the bottom left corner (Fig. 8(a)) is substantially depleted in Cr and thus is blue in color (Fig. 8(b)). However around this primary precipitate, near the γ'/γ interface, a yellow colored interfacial layer is observed which is in between the blue and red contrast. This suggests a progressive decrease in Cr

content from the γ' precipitate to the γ matrix. Again the smaller precipitates in the top right of Fig. 8(a) have intermediate Cr contents (refer to Fig. 6(b)) and are thus yellow in color. Apart from this, Fig. 8(b) also shows nanometer scale pockets within the depleted region that are locally depleted in Cr, as they exhibit a light yellow contrast. However the corresponding Cr isosurface in Fig. 8(a) does not delineate these regions. This indicates that these nanoscale regions have not yet reached the composition of 14at% Cr. These regions are non-spherical in morphology and from the isosurface generated using 18at% Cr, shown in Fig. 8(c), it is clear that the Cr rich and Cr lean regions are interconnected in nature within the γ' depleted region as well as in the regions where the fine scale tertiary (or secondary) precipitates are formed. Thus in this figure all the regions containing less than 18at% Cr are shown in blue, while the regions in between contain more than 18at% Cr. The interconnected nature of these compositionally phase separated regions is a possible indication of a spinodally-decomposed matrix exhibiting a continuous variation in composition, rather than discrete pockets that reach an equilibrium composition via a classical nucleation and growth process [24]. It needs to be re-iterated that the regions that exhibit this continuous network of Cr-depleted pockets are farthest away from the equilibrium γ composition, and presumably form at the highest undercooling. Thus, as expected, these interconnected regions are not present near the precipitate-free depletion zone, which seem to be closer to the equilibrium composition of the γ matrix.

This proposition can be further strengthened using the composition profiles that were discussed in Fig. 6. Comparing the proxigrams generated from primary and secondary (or tertiary) precipitates it is evident that the former exhibits a sharper interface when compared to the later. This is in accordance with the prediction of Cahn et.al. [24] where it is mentioned that at lower supersaturations (lower undercooling) the nucleus behaves classically and the region around this classical nucleus approaches an equilibrium composition. However as supersaturation increases, as in the case for smaller γ' particles, the nucleus starts losing its resemblance to a classical nucleus. Thus at higher undercooling, both Helmholtz free energy as well as gradient energy factors contribute to the diffuseness of the interface. Also no part of this nucleus is approximately homogeneous and the composition of its center is less than that of a classical nucleus. This is synonymous to a system that undergoes phase separation via spinodal decomposition, where the composition fluctuation is small in degree and large in extent.

Growth influenced Morphology and Chemical changes

Fig. 9(a) shows a three-dimensional (3D) atom probe reconstruction of the slow cooled and 760°C/1 hr aged (SC1) sample. The 160nm X 100nm X 100nm reconstruction, generated using a Cr isosurface (blue) superimposed on Ni ions (green), clearly shows primary as well as smaller tertiary γ' precipitates. Similar to the SC0 condition shown in Fig. 5, the depletion zone between precipitates of two different generations is clearly visible in this reconstruction. The overall size of these precipitates was determined using the IVASTM software and their equivalent diameters have been plotted in Fig. 9(b). Similar to the studies conducted in case of the SC0 sample, the first and second generation of primary and secondary γ' precipitates were imaged using SEM and EFTEM

respectively (not shown) and subsequently their size distributions were measured. The compilation of this data, containing the equivalent diameters of three different γ' generations, obtained using three different characterization tools, is shown in Fig. 10(a). Unlike in SC0 condition (Fig. 4), this size distribution plot clearly shows three distinct populations (or size scales) of γ' precipitates, suggesting three distinct nucleation bursts corresponding to different undercooling values below the γ' solvus temperature. Fig. 10(b) shows a proximity histogram generated using the Cr isosurface that shows the variation of primary alloying elements in Rene 88DT after aging for 1 hr at 760°C (SC1). Similar to the SC0 condition (Fig. 7), on moving away from the γ'/γ interface, while the near field γ composition has reached equilibrium, the far-field γ composition is far-from equilibrium and contains lower than equilibrium amounts of Cr and Co, and supersaturation of Al and Ti. Incidentally comparing Figs. 9(a) and 10(b), the γ compositions that were probed 20nm beyond the γ'/γ interface in both cases was in the vicinity of tertiary γ' precipitates.

Similar studies were conducted on Rene 88DT samples that were aged for 15 hours. Fig. 11(a) shows an EFTEM image of the alloy that was aged for 15 hours at 760°C after solutionizing and slow cooling to room temperature (SC15). From Fig. 11(a) as well as the higher magnification image in Fig. 11(b), it is clear that the smaller γ' precipitates are coarser than those in the SC0 condition. However, very limited changes are observed in the size of primary γ' precipitates or the depleted zone around them. Atom probe tomography was conducted with the SC15 sample so as to obtain the true morphology and size of the tertiary (or secondary) γ' precipitates and are shown in Fig. 12. As seen from the isosurfaces, generated using 14 at% Cr (blue), superimposed on Ni atoms (green) (Fig. 12 (a)), the γ' precipitates have grown and are ~20nm in diameter after 15 hours of aging. Also the size of the γ' precipitates closest to the primary precipitate appear to be smaller than the precipitates present at further distances from the primary precipitate indicating the development of three distinct populations, primary, secondary, and tertiary. The long-range composition profiles for the alloying elements across the primary γ'/γ interface into the precipitate free depleted zone have been plotted by averaging across a cylindrical region of interest (ROI) as shown in Fig. 12(b). These profiles clearly show that for all alloying elements the compositional profile within the precipitate free depleted zone remains constant, clearly indicating that the far-field γ matrix has reached its equilibrium composition in this case. Consequently, there is no supersaturation of Al and Ti (or undersaturation of Cr and Co) present within the matrix that can lead to nucleation or growth of additional γ' precipitates.

Mechanism of multiple bursts of nucleation

Based on the detailed experimental results presented in this paper it is now possible to develop a mechanistic model leading to the multiple nucleation bursts of γ' precipitates during continuous cooling of a nickel base superalloy. During cooling, due to the continuous decrease in temperature below the γ' solvus, there is an associated increase in the thermodynamic driving force for nucleation associated with the continuously increasing undercooling. However as soon as the first generation of γ' precipitates are

nucleated, this driving force is partially consumed, especially in the local region surrounding the first-generation (or primary) precipitates. Thus, the region surrounding these primary γ' precipitates is depleted in γ' forming elements, Al and Ti, and enriched in γ stabilizing elements, Co and Cr. Since the first nucleation burst occurs at relatively high temperatures (low undercooling below the γ' solvus), the higher diffusivity of the various alloying elements promotes their rapid partitioning between the γ' precipitate and the adjacent γ matrix. Also at these high temperatures, the primary γ' precipitates grow quite rapidly and develop a cuboidal to irregular morphology (Figs. 2 and 3) as anisotropic elastic strain energy starts dominating over the isotropic interfacial energy. However as temperature decreases, due to the reduced mobility of the solute elements, their redistribution becomes more and more difficult. Thus a condition similar to the schematic diagram in Fig. 13(a) occurs where the composition close to the primary γ' precipitates reaches equilibrium (as suggested by a decrease in Al and increase in Cr). However as one probes away from the precipitate, far-field into the γ matrix, there is an enrichment of Al (and Ti) and depletion of Cr (and Co), primarily because of the inability of these regions to equilibrate rapidly at low temperatures (Fig. 13(a)). This results in the formation of far-field supersaturated corridors within the γ matrix, that act as potential sites for γ' nucleation at lower temperatures when the relative driving force increases. Thus, at these lower temperatures, the higher thermodynamic driving force and higher nucleation rate result in a second nucleation burst leading to a large number density of γ' precipitates, increasing the γ' volume fraction (corresponding to the increase in (001) γ' to (111) $\gamma' + \gamma$ peak intensity ratio in Fig. 1). On further cooling these particles try to grow but their growth is severely restricted due to the low diffusivities. Thus the second generation of precipitates has a higher number density and is smaller than the first generation of precipitates (Fig. 4). Furthermore, this high number density of secondary precipitates leads to small inter-precipitate distances and consequently results in rapid overlap of the diffusion fields (soft impingement), restricting their further growth. These precipitates are small enough such that the isotropic interfacial energy dominates over anisotropic elastic strain energy. This coupled with the inherently low γ - γ' misfit in case of Rene'88DT, results in these secondary precipitates maintaining a near spherical morphology (Figs. 3 and 5). Also as discussed earlier, these secondary precipitates do not exhibit features of a classically nucleated precipitate of equilibrium composition, but rather exhibit both compositional inhomogeneities within the precipitates as well as relatively diffuse γ'/γ interfaces (Fig. 6). Changes also take place in the γ matrix that surround these precipitates. Thus the matrix becomes depleted in Al (and Ti) and enriched in Cr (and Co), as shown in the schematic diagram in Fig. 13(b). Thus at this temperature the region close to the secondary γ' precipitates have a very low driving force for further nucleation. However Fig. 13(b) also shows that the γ matrix between the secondary γ' and the depleted zone (around the primary γ') still retains a non-equilibrium composition, involving, for example, an Al supersaturation (or Cr undersaturation). However the thermodynamic driving force is not sufficient to cause any fresh nucleation until a really large undercooling is achieved. This undercooling occurs when the sample is cooled to further lower temperatures that leads to a third burst of nucleation resulting in the population of tertiary γ' precipitates (schematic diagram in Fig. 13(c)). However, slower kinetics and limited supersaturation of solute at this stage further limit the growth

of these tertiary γ' precipitates. Thus a large number of fine scale spherical γ' precipitates are formed. It should be noted that typically the tertiary γ' precipitates are nucleated in between the primary and secondary γ' precipitates but closer to the secondary precipitates, primarily because the depletion zone around a secondary γ' precipitate is much smaller than that of primary γ' precipitate (Fig. 13(c)). Summarizing, several thermodynamic and kinetic factors such as driving force for nucleation, number density of nucleation sites (related to the nucleation rate), and diffusivity determine the formation of multiple generations of γ' precipitates and the complex interplay of these factors give rise to the multi-scale microstructures that are experimentally observed on continuous cooling. These observations are in excellent agreement with the phase field simulations reported previously [10] as well as with experimental investigations in some commercial nickel base superalloys [6,9,12], where continuous cooling results in shrinkage of diffusion fields associated with larger γ' precipitates, consequently opening up precipitate free supersaturated γ channels where further nucleation events can take place.

Summary and Conclusions

This paper presents a detailed investigation of multi-modal size distribution of γ' precipitates developing in nickel base superalloys as a result of the phenomena of multiple γ' nucleation bursts during continuous cooling of the alloy from above the γ' solvus temperature. The salient and novel findings of this paper can be summarized as follows:

1. This paper presents direct evidence of multiple γ' nucleation bursts during continuous cooling based on in situ synchrotron-based x-ray diffraction results where these nucleation bursts have been captured in real time.
2. Coupling multiple characterization techniques, SEM, TEM (energy-filtered TEM), and APT, the size distribution of three distinct populations of γ' precipitates, resulting from these nucleation bursts, have been quantified.
3. The experimental evidence, based primarily on APT investigations coupled with energy-filtered TEM studies, clearly reveals the coupled thermodynamic and kinetic (diffusion) rationale for the formation of γ' -depleted precipitate-free zone adjacent to the first-generation of γ' precipitates formed. Thus, while local compositional equilibrium is achieved near the γ'/γ interface of these first-generation precipitates, the continuous cooling process does not permit the longer range far-field γ composition to equilibrate, consequently leading to a higher supersaturation in the matrix at lower temperatures eventually resulting in the next nucleation burst. This explanation is a direct experimental validation of the phase-field models discussed previously.
4. Based on the experimental evidence presented in this paper, the rationale for the formation of the third generation of γ' precipitates in between the first and second generation of precipitates has been clearly explained.
5. The experimental results lead to some fundamental questions regarding the differences in the precipitation mechanisms of first-generation γ' precipitates (at lower undercooling or higher temperature) versus the second or third-generation of γ'

precipitates (at higher undercooling or lower temperature). Thus, while the first-generation of precipitates appear to follow a classical nucleation and growth pathway, the second (or third) generation of precipitates exhibit features of a far-from equilibrium non-classical mechanism of precipitation. On formation, these second (or third) generation precipitates exhibit far-from equilibrium compositions and compositionally diffuse γ'/γ interfaces with large widths.

6. Isothermal annealing of the continuously-cooled alloy at 760°C results in the compositional equilibration of both γ' precipitates as well as the γ matrix and the long-range non-equilibrium diffusion profiles are obviated.

Future studies will involve a more detailed investigation of the formation mechanism of second or third generation γ' precipitates in these alloys, that typically form at high undercooling (low temperature) and could therefore exhibit far-from equilibrium non-classical precipitation behavior. Such non-classical characteristics of the second or third generation precipitates can have a significant impact on the nature of the γ'/γ interface which in turn directly impacts the high temperature microstructural stability (coarsening behavior) as well as the mechanical properties of these alloys.

Acknowledgements

The authors would like to acknowledge the U. S. Air Force Research Laboratory (AFRL ISES contract FA8650-08-C-5226) for providing financial support for this study. In addition, the authors also gratefully acknowledge the Center for Advanced Research and Technology (CART) at the University of North Texas and the Center for the Accelerated Maturation of Materials (CMM) at the Ohio State University for access to the experimental facilities used for this study.

References

1. R. J. Mitchell, M. Preuss, *Metall. Mater. Trans. A*, 2007, vol. 38, pp. 615-27.
2. R. C. Reed, *The Superalloys: Fundamentals and Applications*, Cambridge University Press, Cambridge, U.K. (2006).
3. D. D. Krueger, R. D. Kissinger, R. D. Menzies, and, C. S. Wukusick, *U. S. Patent* 4,957,567.
4. D. D. Krueger, R. D. Kissinger, and, R. D. Menzies, *Superalloys 1992*, Ed. S. D. Antolovich et. al., TMS-AIME, Warrendale, PA, 1992, pp. 277-86.
5. S. T. Wlodek, M. Kelly, and, D. A. Alden, *Superalloys 1996*, Ed. R. D. Kissinger, D. J. Deye, D. L. Anton, A. D. Cetel, M. V. Nathal, T. M. Pollock, and, D. A. Woodford, TMS, Warrendale, PA, 1996, pp.129-36.
6. S.S. Babu, M.K. Miller, J.M. Vitek, S.A. David, *Acta Mater.*, **49** (2001) 4149.
7. J. Y. Hwang, R. Banerjee, J. Tiley, R. Srinivasan, G. B. Viswanathan, H. L. Fraser, *Metall. Mater. Trans. A*, **40** (2008) 24.
8. D. N. Seidman, C. K. Sudbrack, and, K. E. Yoon, *JOM*, **58** (2006) 34.
9. P. M. Sarosi, B. Wang, J. P. Simmons, Y. Wang, and, M. J. Mills, *Scripta Mater.*, **57** (2007) 767.
10. Y. H. Wen, J. P. Simmons, C. Shen, C. Woodward, and, Y. Wang, *Acta Mater.*, **51** (2003) 1123.
11. Y. H. Wen, B. Wang, J. P. Simmons, and, Y. Wang, *Acta Mater.*, **54** (2006) 2087.
12. R. Radis, M. Schaffer, M. Albu, G. Kothleitner, P. Polt, E. Kozeschnik, *Acta Mater.* **57** (2009) 5739-5747.
13. A.R.P. Singh, S. Nag, J.Y. Hwang, G.B. Viswanathan, J. Tiley, R. Srinivasan, H.L. Fraser and R. Banerjee, *Mater. Char.*, **62**(9) (2011) 878.
14. G. Boussinot, A. Finel and, Y. Le Bouar, *Acta Mater.*, **57** (2009) 921.
15. M. K. Miller, *Micron*, 2001, vol. 32, pp.757-64.
16. D. Blavette, E. Cadel, and, B. Deconihout, *Mater. Char.* 2000, vol. 44, pp.133-57.
17. M.K. Miller, A. Cerezo, M.G. Hetherington and G. D. W. Smith, *Atom Probe Field Ion Microscopy*, Oxford University Press, Oxford, England, (1996) 476-483.
18. J. MacSleyne, M.D. Uchic, J.P. Simmons and M. De Graef, *Acta Mater.*, **57** (2009) 6251.
19. P. M. Sarosi, G. B. Viswanathan, D. Whitis, and, M. J. Mills, *Ultramicroscopy*, 2005, vol. **103**, pp. 83-93.
20. Littles, Jr., J.W., Pettit, R.G., Schirra, J.J., Cowles, B.A., Holmes, R.A., Russ, S.M., Rosenberger, H., Larsen, J.M., in *Materials Damage Prognosis*, TMS Publications, Warrendale, PA, 23-29 (2005).
21. K. Thompson, D. Lawrence, D. J. Larson, J. D. Olson, T. F. Kelly, and, B. Gorman, *Ultramicroscopy*, 2007, vol.107, pp. 131.
22. J. Tiley, R. Srinivasan, R. Banerjee, G. B. Viswanathan, B. Toby and H.L. Fraser, *Mat. Sci. Tech.*, **25**(11) (2009) 1369.
23. O.C. Hellman, J.A. Vandenbroucke, J. Rusing, D. Isheim, D.N. Seidman, *Micro. Micro.*, **6** (2000) 437.
24. J.W. Cahn, J.E. Hilliard, *J. Chem. Phys.*, **31** (1959) 688.

Figure Captions:

Fig. 1 Progressive change in the intensity of (a) (001) γ' superlattice, and (b) (111) fundamental reflections arising from both γ and γ' phases as a function of temperature during slow continuous cooling of Rene 88 DT alloy (SC0) from the single γ phase field. (c) A plot showing the ratio of (001) γ' to (111) $\gamma' + \gamma$ peak intensities over a range of temperature.

Fig. 2 (a) Low and (b) high magnification backscatter SEM images of the SC0 sample with primary γ' precipitates exhibiting a darker contrast.

Fig. 3 (a) Low and (b) high magnification energy-filtered transmission electron microscopy images obtained using Cr M-edge in the electron energy-loss spectroscopy spectrum of the SC0 sample. Along with primary γ' precipitates the smaller secondary (and tertiary) γ' precipitates which are Cr-depleted, exhibit the darker grey contrast in these images.

Fig. 4 (a) Precipitate size distribution plot of SC0 sample showing the size difference between the primary γ' and smaller secondary (and tertiary) γ' precipitates. (b) A Gaussian distribution used to fit the curves in (a) in order to determine the average diameter and standard deviation of different generation of precipitates.

Fig. 5 (a) APT reconstruction of Cr (blue) and Al (red) atoms in as slow cooled (SC0) sample. The γ' precipitates are the Al-rich red regions with Cr-rich blue γ matrix. (b) An isosurface of the above reconstruction using 14at% Cr along superimposed on Ni ions, where the γ' precipitates having leaner amount of Cr. The different generations of γ' precipitates are clearly visible. (c) A second example in terms of atom probe reconstruction (Cr=14at% isosurface along with Ni ions) of the same SC0 sample.

Fig. 6 Proximity histograms of (a) primary γ' and (b) secondary (or tertiary) γ' precipitates in SC0 sample using a Cr=14at% isosurface. The plots show the partitioning of the primary alloying elements i.e. Al, Ti, Cr, Co, and Mo between the γ and γ' phases. (c) Plot comparing the Al and Cr compositional profiles across the γ'/γ interface for two specific large (primary) and small (tertiary or secondary) γ' precipitates.

Fig. 7 (a) Proximity histograms of the SC0 sample plotted from a primary γ' precipitate on the left to a precipitate-free γ' depletion zone towards the right. The plot shows the near field and far field compositions of the γ matrix. Magnified images of the above proximity histogram showing the compositional variation of (b) Al and Ti and (b) Cr near and far away from the primary γ' precipitate.

Fig. 8 A 2-D compositional map of Cr, created using a 2nm thick region of interest across primary and tertiary (or secondary) γ' precipitates, along with the depleted zone lying in between them, (a) with and (b) without an overlapping isosurface that was generated using 14at% Cr (showing regions that are equal to or less than 14at% Cr). (c) An

isosurface of the above reconstruction using 18at% Cr, showing the interconnected nature of Cr rich and Cr lean regions.

Fig. 9 (a) APT reconstruction of Cr (blue) and Al (red) atoms in the slow cooled and 1 hr aged (SC1) sample. The γ' precipitates are the Al-rich red regions with Cr-rich blue γ matrix. (b) Precipitate size distribution plot of the tertiary γ' precipitates generated using the IVASTM software.

Fig. 10 (a) Precipitate size distribution plot of SC1 sample showing the size difference between the primary γ' , secondary γ' and tertiary γ' precipitates. (b) Proximity histograms of the SC1 sample plotted from a primary γ' precipitate on the left to the γ matrix towards the right. The plot shows the near field and far field compositions of the γ matrix.

Fig. 11 (a) Low and (b) high magnification energy-filtered transmission electron microscopy images obtained using Cr M-edge in the electron energy-loss spectroscopy spectrum of the SC15 sample. Along with primary γ' precipitates the smaller secondary (and tertiary) γ' precipitates which are Cr-depleted, exhibit the darker grey contrast in these images.

Fig. 12 (a) APT reconstruction of an isoconcentration surface, generated using 14 at% Cr (blue) superimposed on Ni atoms (green), in slow cooled and aged (SC15) sample. (b) A compositional profile, from a small tertiary (or secondary) to large primary γ' precipitate with the depletion zone lying in between them, showing the variation of major alloying additions in SC15 sample.

Fig. 13 (a)-(c) Schematic illustrations of how multiple γ' generations can form during slow cooling of Rene 88DT alloy.

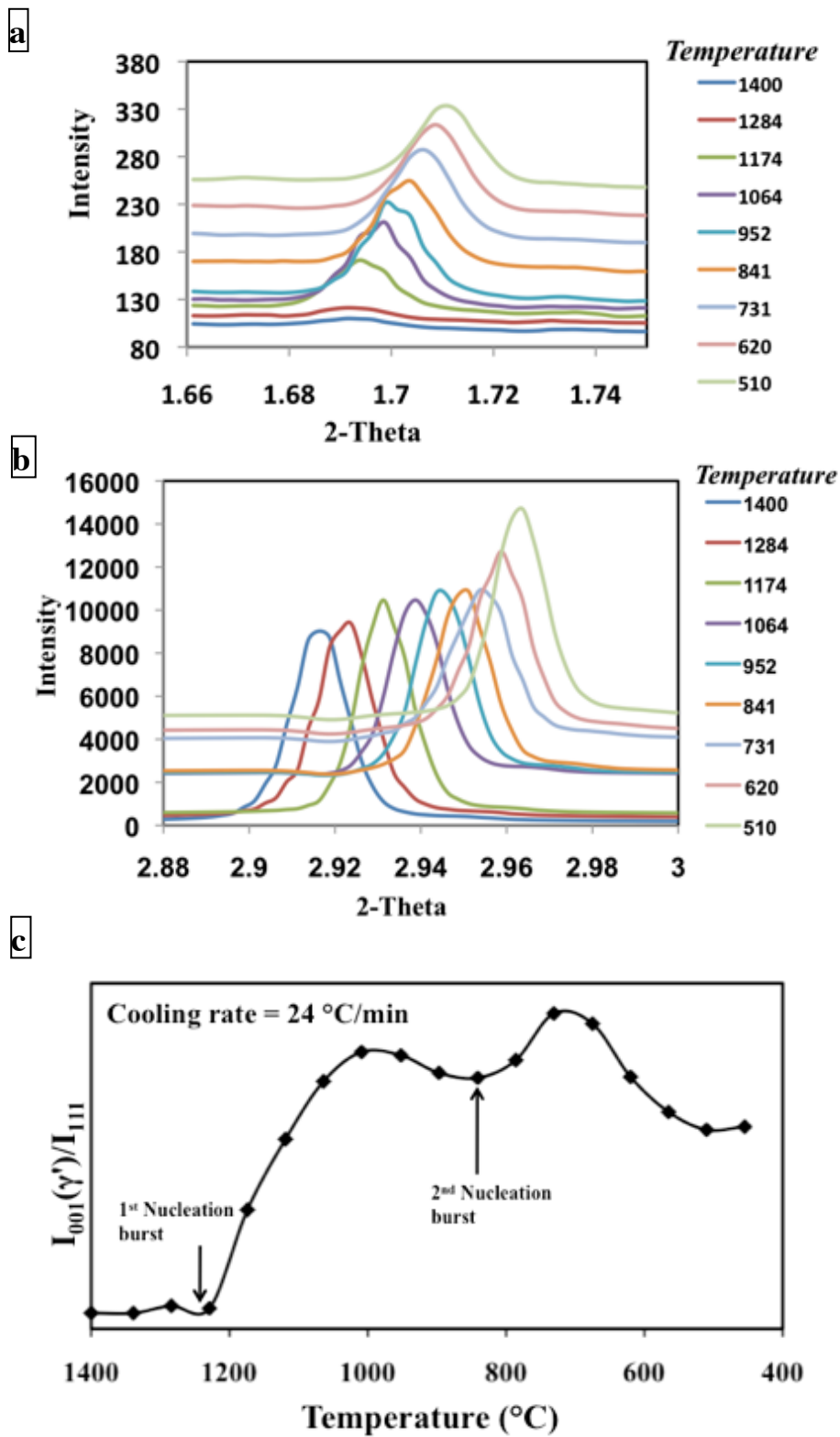


Fig. 1

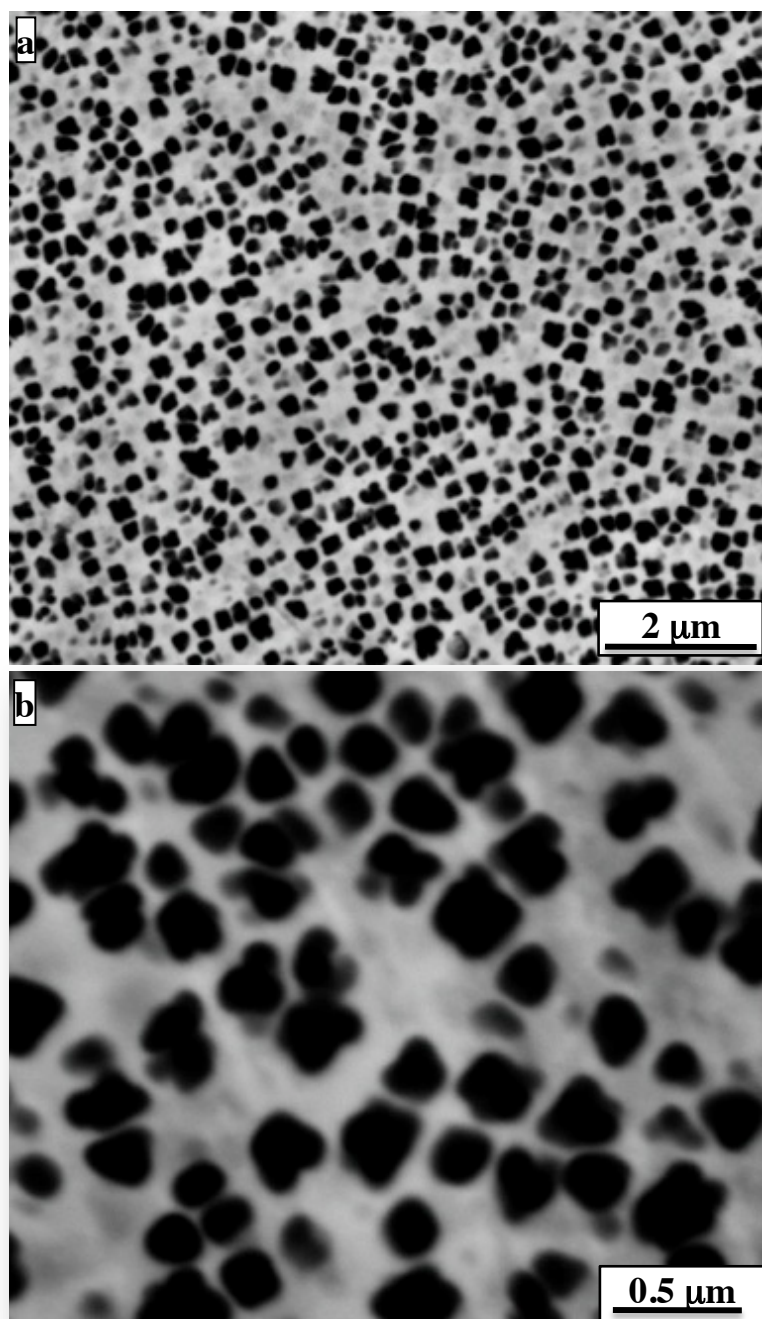


Fig. 2

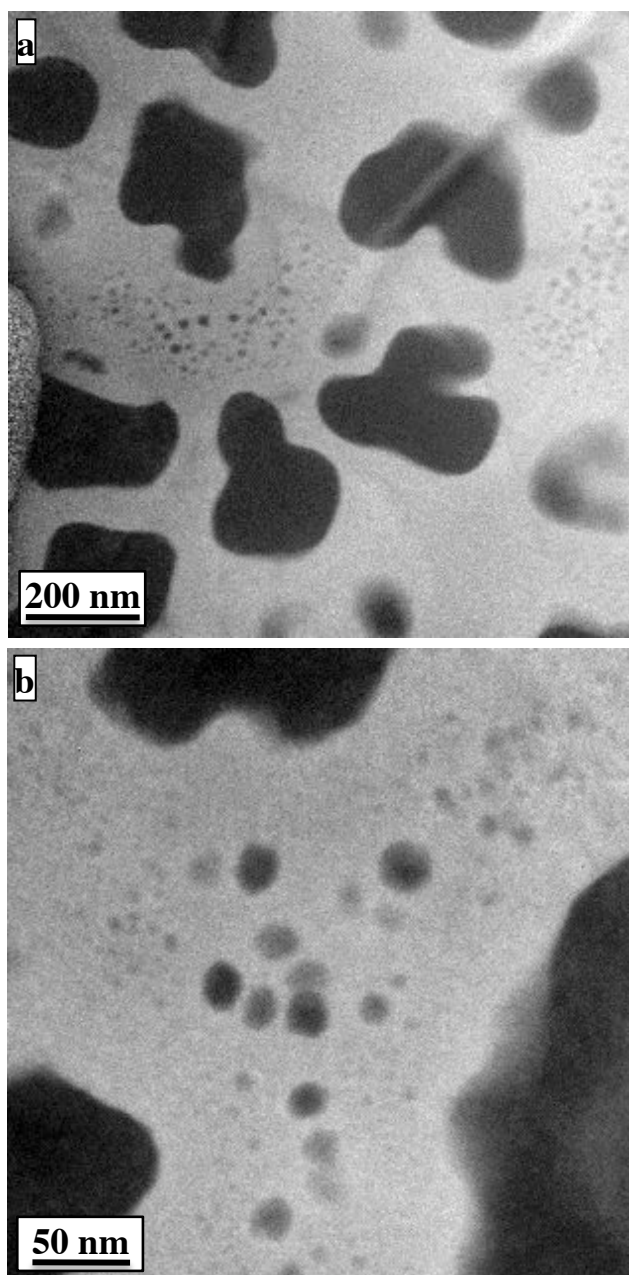


Fig. 3

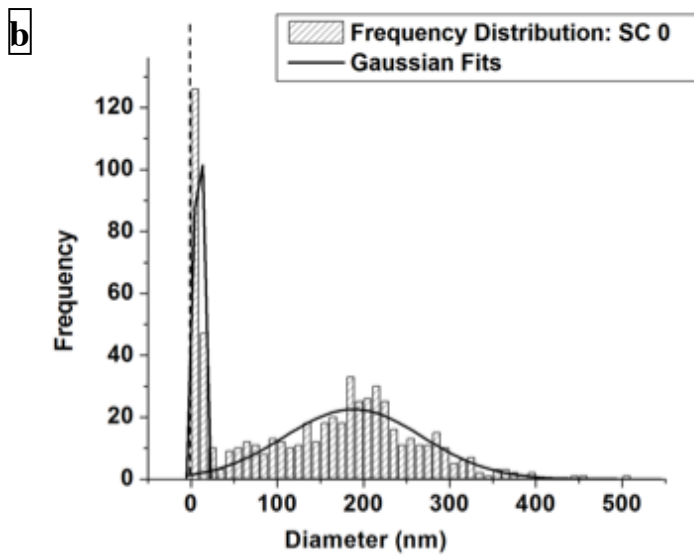
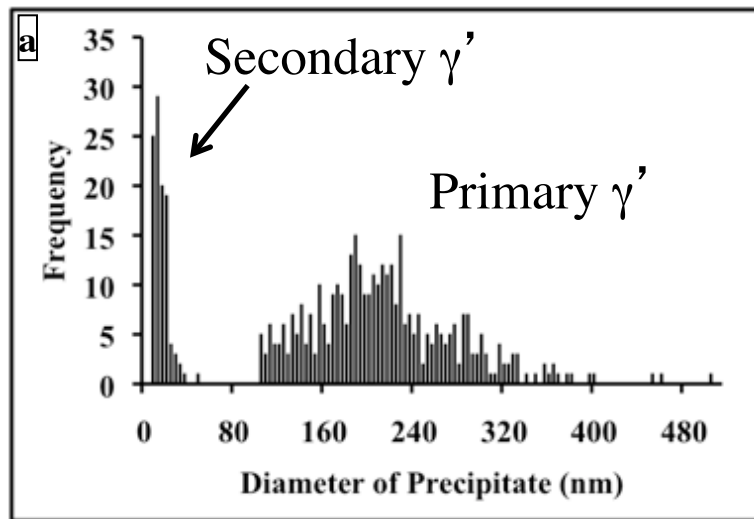


Fig. 4

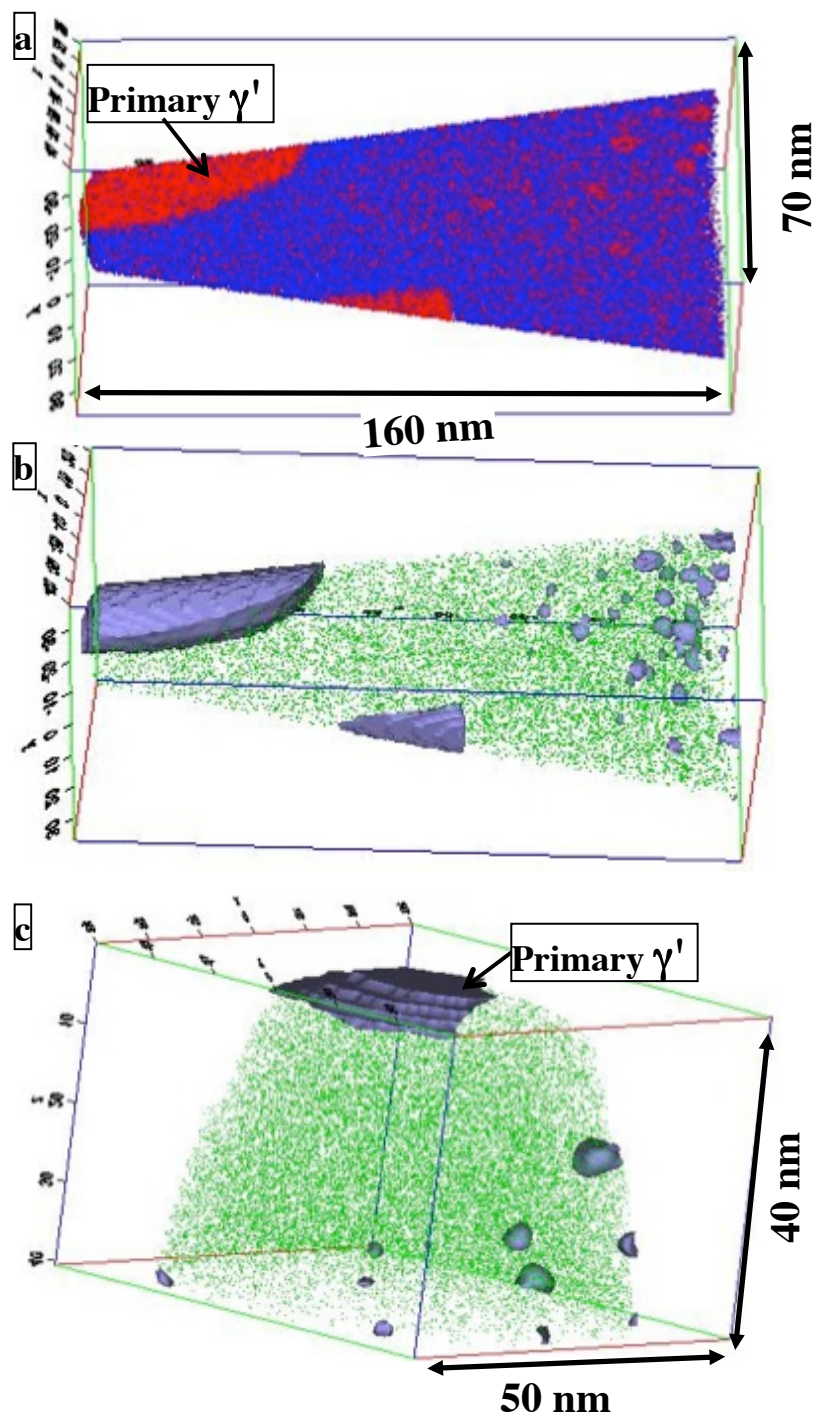


Fig. 5

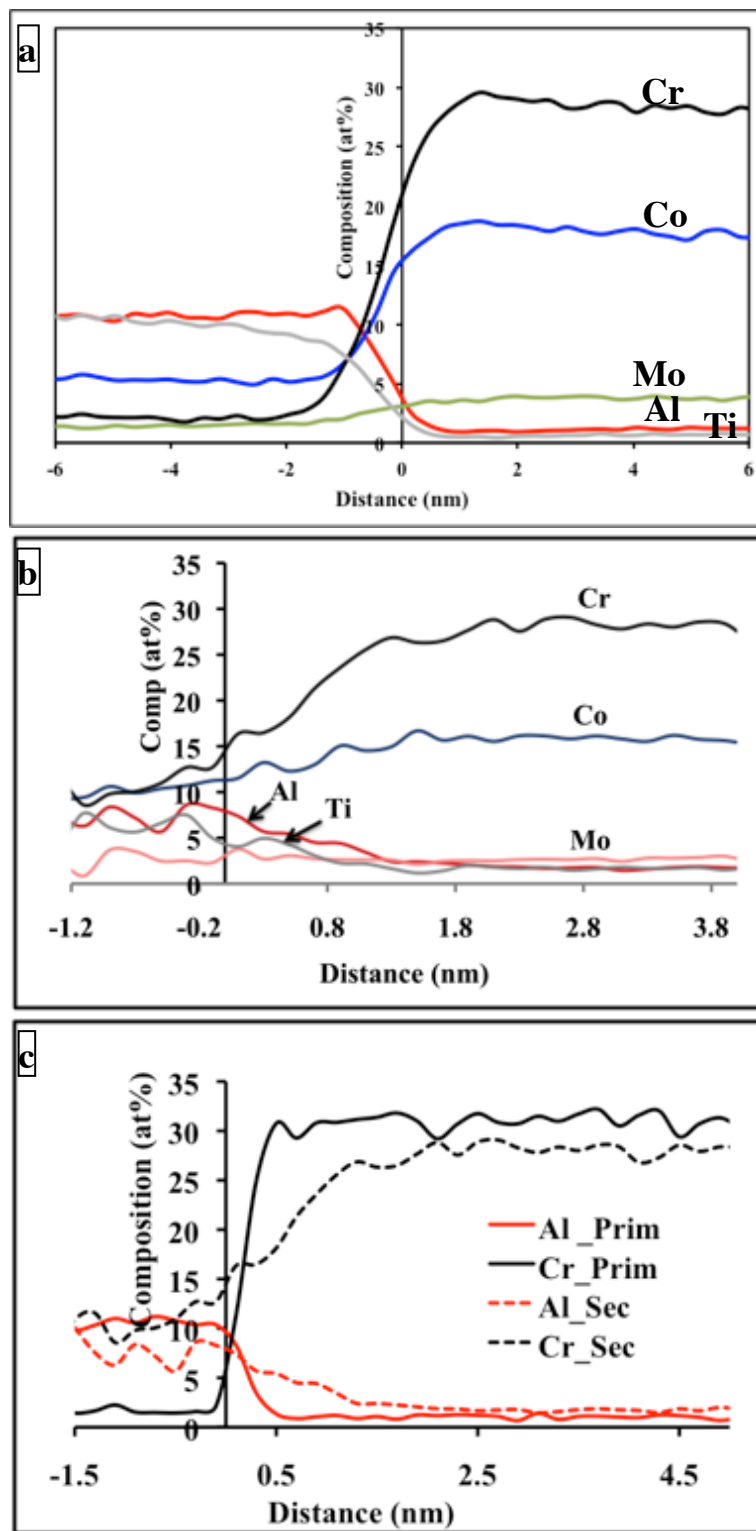


Fig. 6

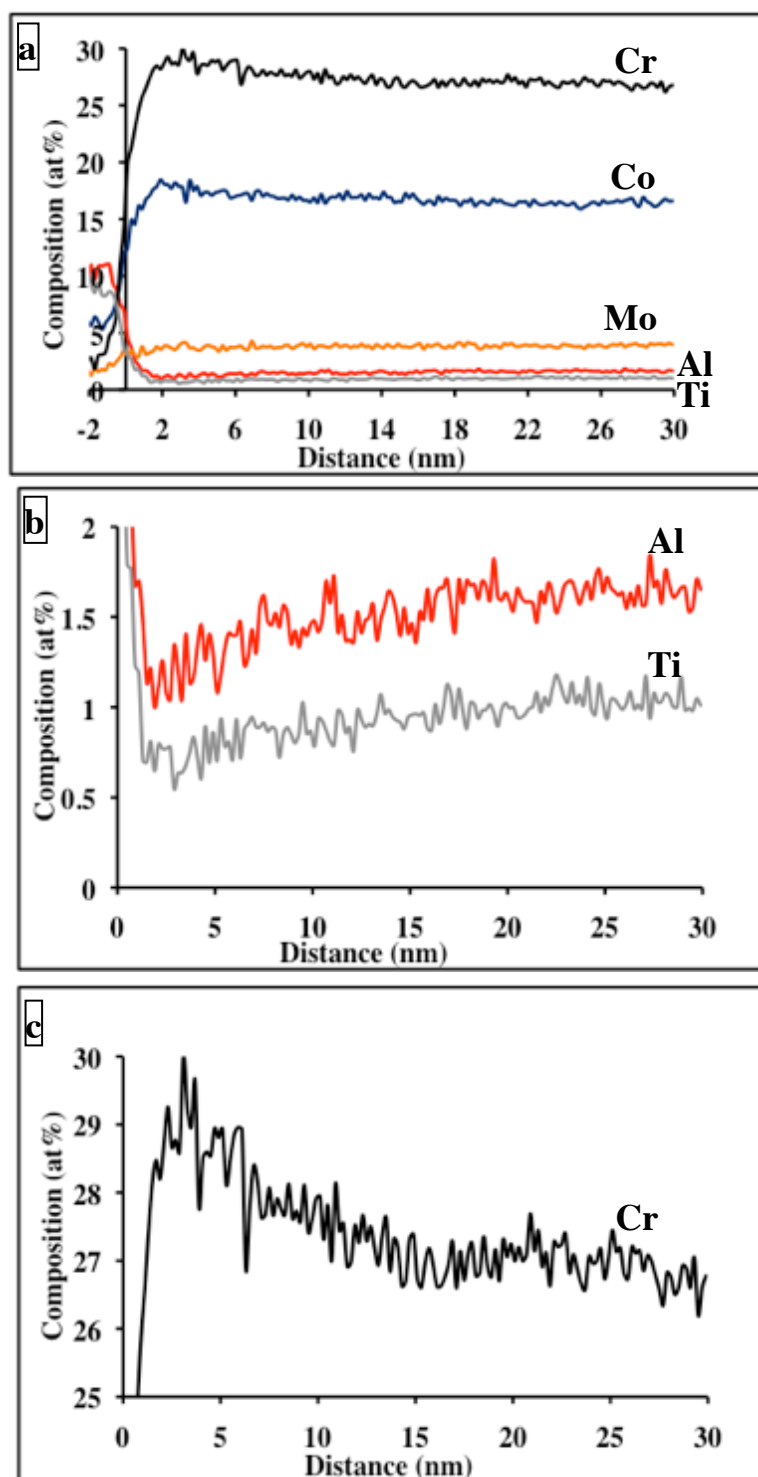


Fig. 7

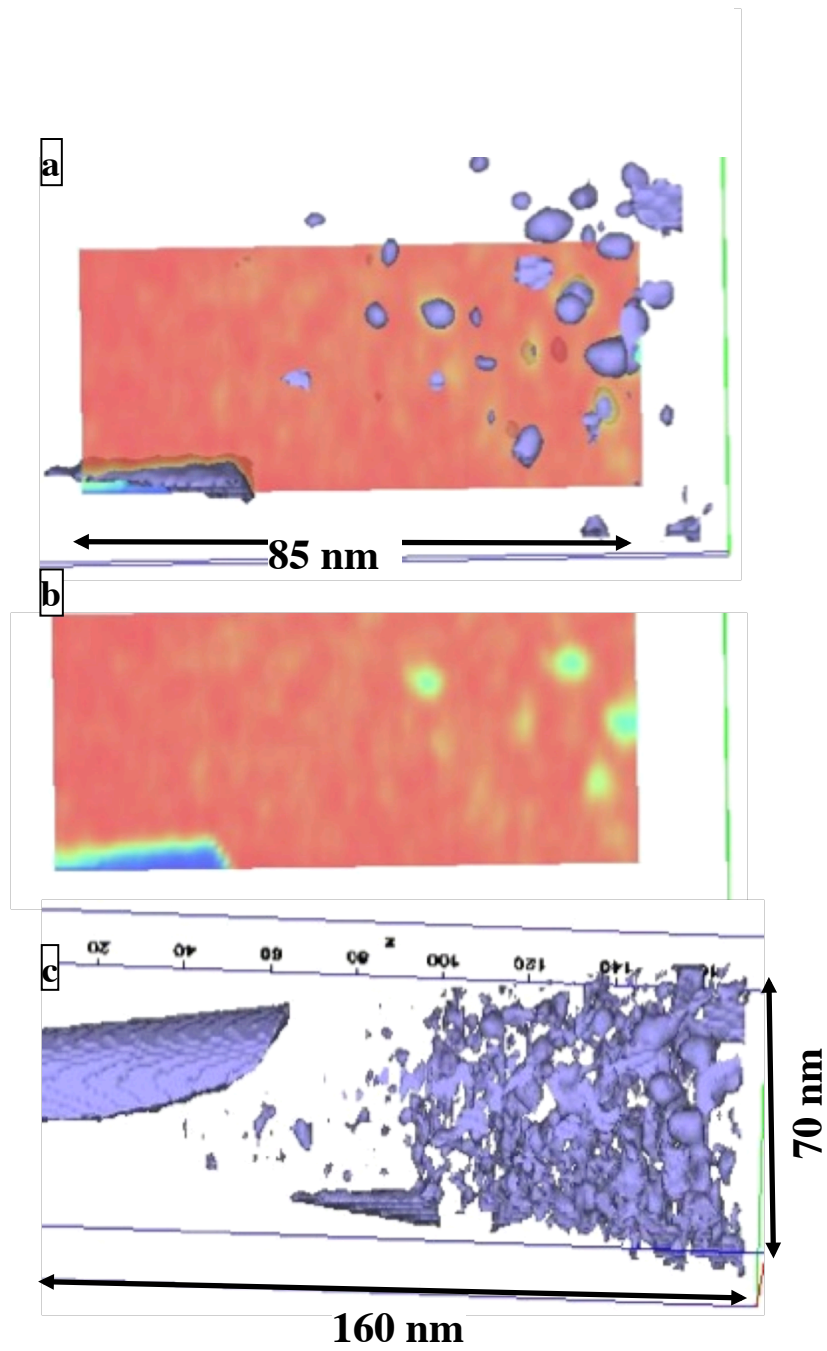


Fig. 8

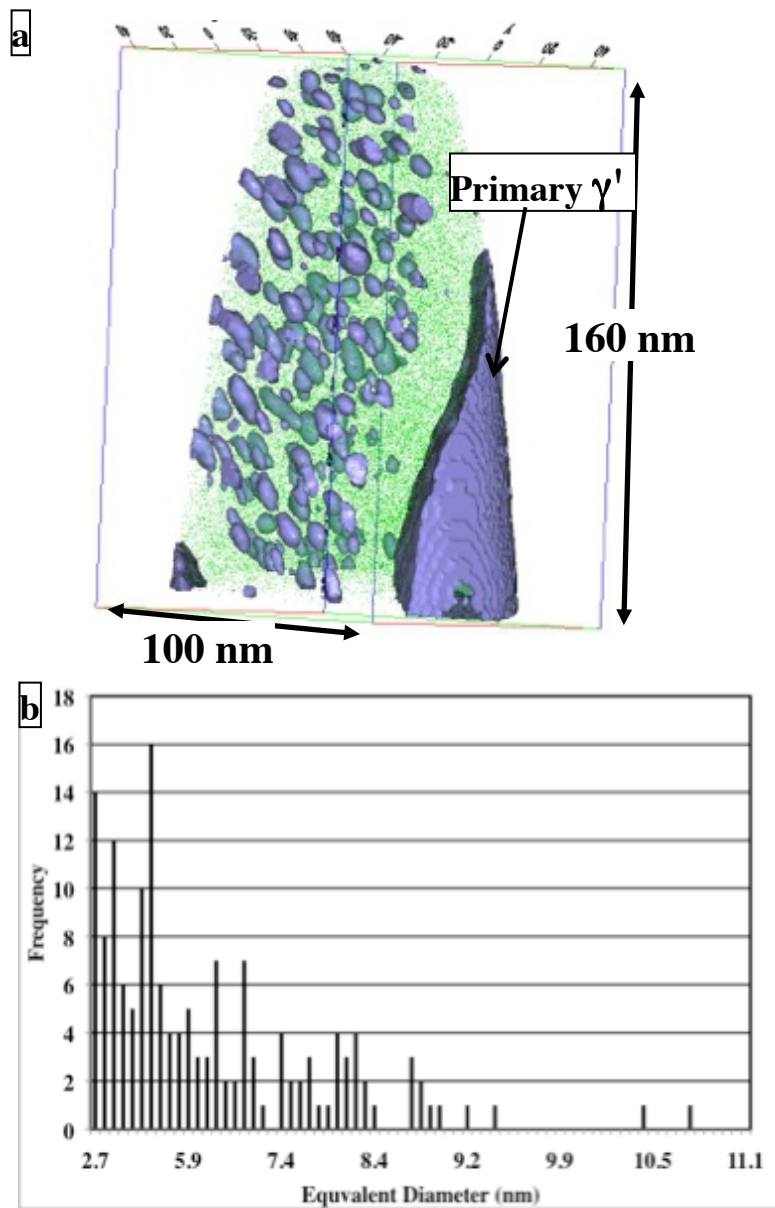


Fig. 9

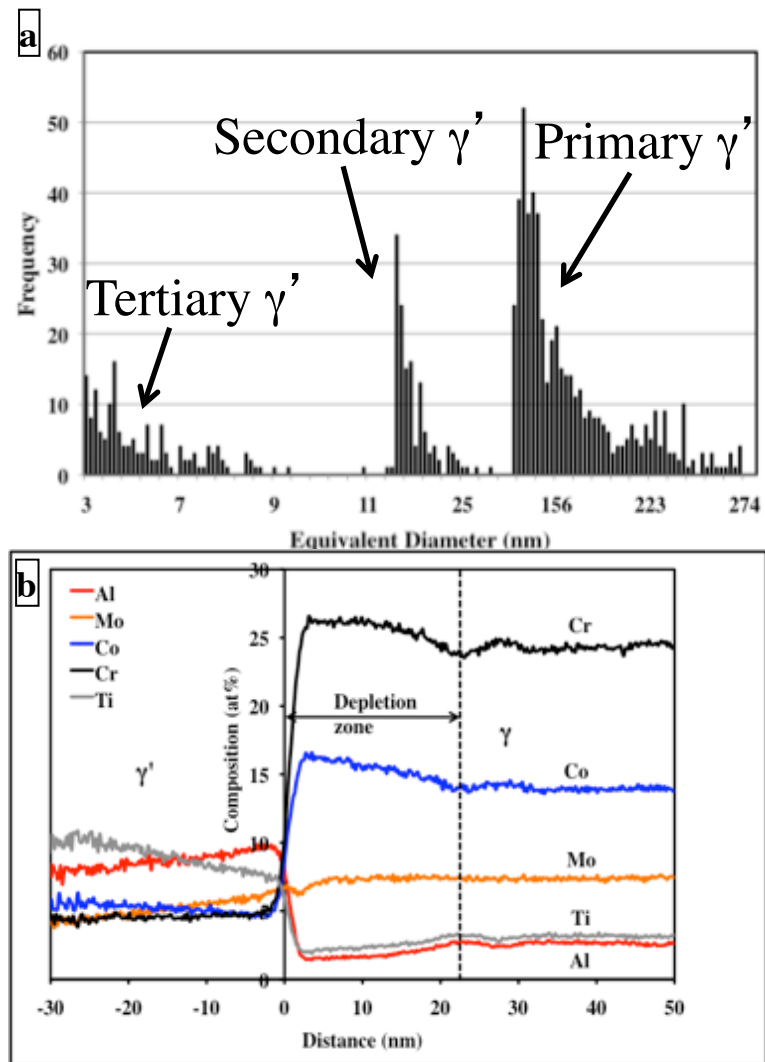


Fig. 10

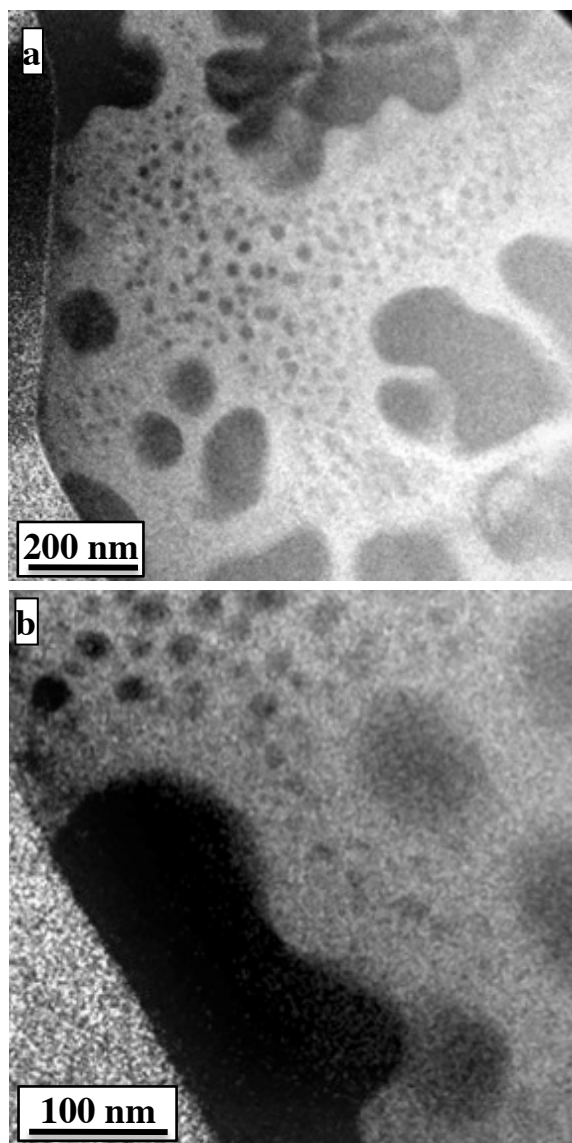


Fig. 11

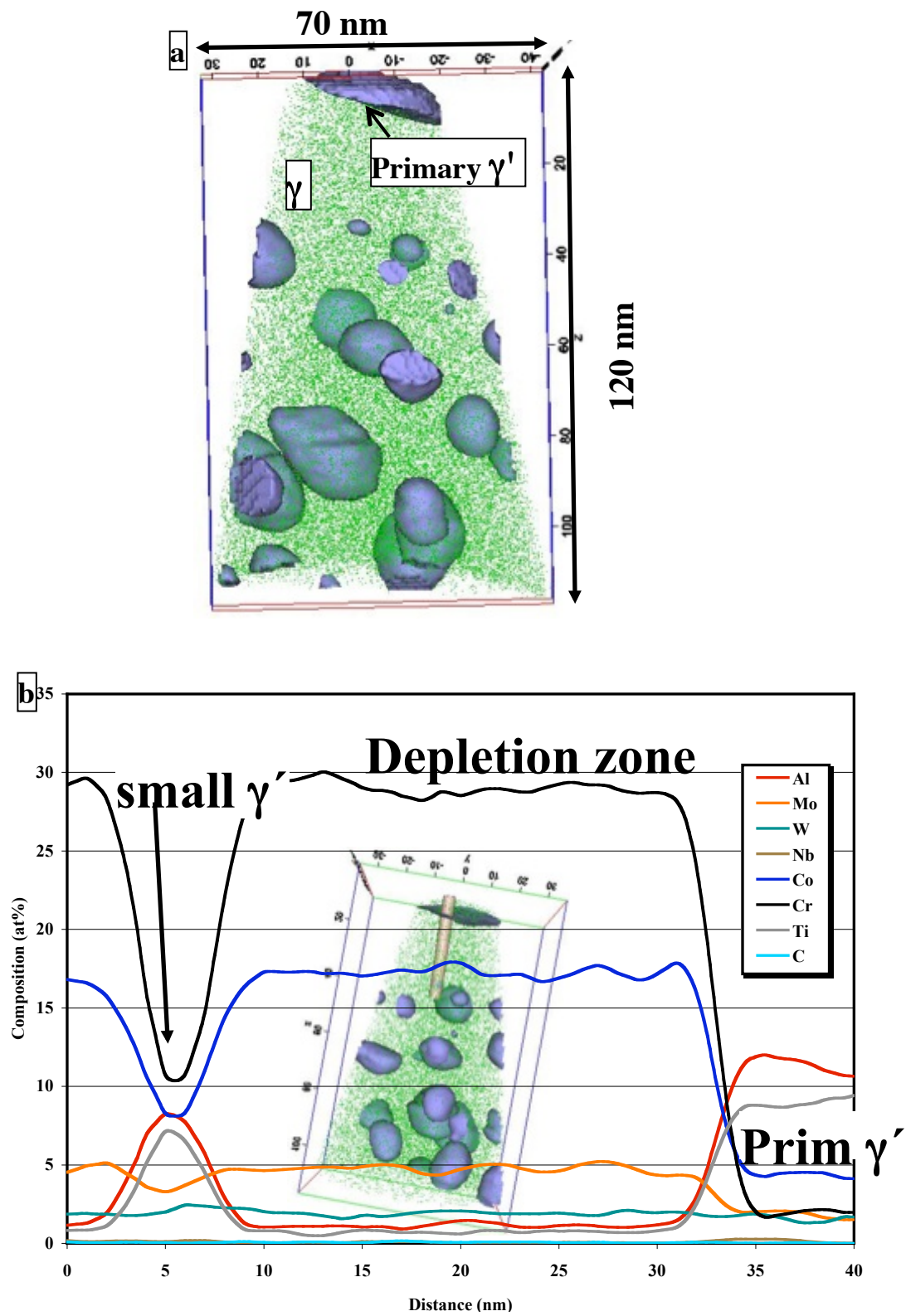


Fig. 12

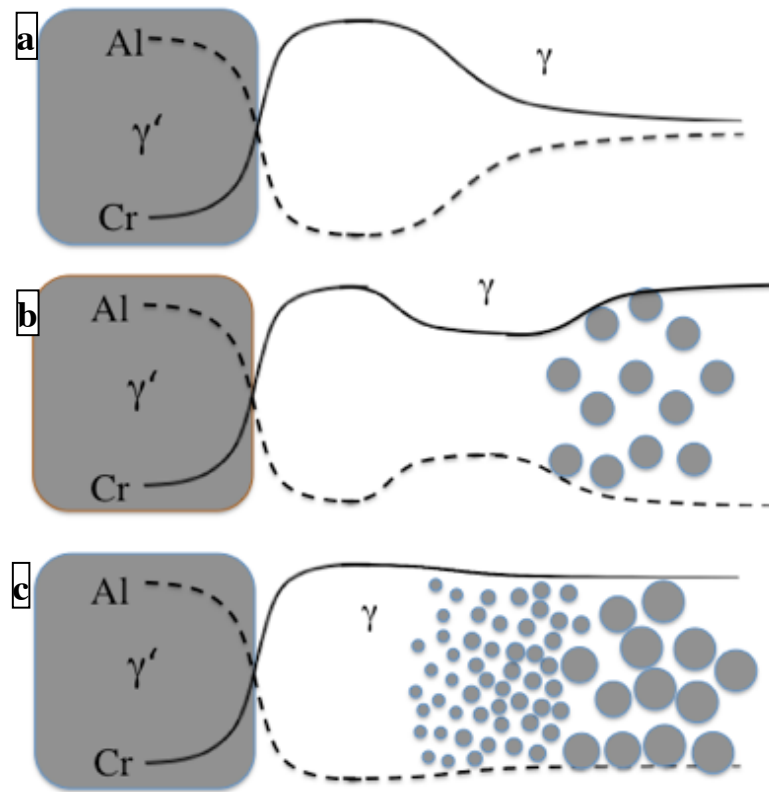


Fig. 13